Graphene Quantum Sheet Catalyzed Silicon Photocathode for Selective CO_2 Conversion to CO

Ki Dong Yang, Yoonhoo Ha, Uk Sim, Junghyun An, Chan Woo Lee, Kyoungsuk Jin, Younghye Kim, Jimin Park, Jung Sug Hong, Jun Ho Lee, Hye-Eun Lee, Hui-Yun Jeong, Hyungjun Kim, and Ki Tae Nam**

The reduction of carbon dioxide (CO_2) into chemical feedstock is drawing increasing attention as a prominent method of recycling atmospheric CO_2. Although many studies have been devoted in designing an efficient catalyst for CO_2 conversion with noble metals, low selectivity and high energy input still remain major hurdles. One possible solution is to use the combination of an earth-abundant electrocatalyst with a photoelectrode powered by solar energy. Herein, for the first time, a p-type silicon nanowire with nitrogen-doped graphene quantum sheets (N-GQSs) as heterogeneous electrocatalyst for selective CO production is demonstrated. The photoreduction of CO_2 into CO is achieved at a potential of –1.53 V versus Ag/Ag^+, providing 0.15 mA cm^{-2} of current density, which is 130 mV higher than that of a p-type Si nanowire decorated with well-known Cu catalyst. The faradaic efficiency for CO is 95%, demonstrating significantly improved selectivity compared with that of bare planar Si. The density functional theory (DFT) calculations are performed, which suggest that pyridinic N acts as the active site and band alignment can be achieved for N-GQSs larger than 3 nm. The demonstrated high efficiency of the catalytic system provides new insights for the development of nonprecious, environmentally benign CO_2 utilization.

1. Introduction

The development of artificial photosynthetic systems for reducing atmospheric CO_2 into hydrocarbons and alcohols is one of the most urgent issues in alternative energy research due to the rapid increase in CO_2 emissions and the declining supply of fossil fuels.[1–10] Thus far, recycling CO_2 into renewable carbon-based fuels has been solely dependent on biomass, which has inherent problems of low productivity and limited product.[3] To produce various chemicals with high yield, the direct conversion of CO_2 by simply applying electric power is more feasible. However, achieving high selectivity with low overpotential remains challenging in CO_2 reduction due to the closely positioned thermodynamic energies required for each reaction and the kinetic barrier to activation of the CO_2 molecule.[11,12] Although rare-earth metals such as Au, Re, and Rh, as well as their complexes, have been intensively studied to achieve those requirements,[13–17] their application on the industrial scale is difficult.[18,19] With respect to cost and environmental ramifications, developing an efficient and inexpensive CO_2-reducing catalyst has a great impact on CO_2 utilization. Here, for the first time, we demonstrate a p-type Si-based solar-driven CO_2 conversion on a metal-free catalyst in a heterogeneous system. Nitrogen-doped graphene quantum sheets (N-GQSs) enhance the performance of the silicon photocathode by significantly decreasing the overpotential and by providing high selectivity for the conversion of CO_2 to CO.

CO_2 can be reduced to form carbon monoxide (CO), formate (HCOOH), methane (CH_4), or other hydrocarbons at moderate potentials of around –0.2 to –0.6 V versus the normal hydrogen electrode (NHE). Those reactions are listed as follows with their thermodynamic redox potentials (V vs. NHE)

$$CO_2 + 2H^+ + 2e^- \rightarrow CO + H_2O - 0.53 \text{ versus NHE} \quad (1)$$

$$CO_2 + 2H^+ + 2e^- \rightarrow HCOOH - 0.61 \text{ versus NHE} \quad (2)$$

$$CO_2 + 4H^+ + 4e^- \rightarrow HCHO + H_2O - 0.48 \text{ versus NHE} \quad (3)$$

$$CO_2 + 6H^+ + 6e^- \rightarrow CH_3OH + H_2O - 0.38 \text{ versus NHE} \quad (4)$$

$$CO_2 + 8H^+ + 8e^- \rightarrow CH_4 + H_2O - 0.24 \text{ versus NHE} \quad (5)$$

K. D. Yang, U. Sim, J. An, C. W. Lee, K. Jin, Y. Kim, J. Park, J. S. Hong, J. H. Lee, H.-E. Lee, H.-Y. Jeong, Prof. K. T. Nam
Department of Materials Science and Engineering
Seoul National University
Seoul 151-744, South Korea
E-mail: nkitae@snu.ac.kr

Y. Ha, Prof. H. Kim
Graduate School of EEWS
Korea Advanced Institute of Science and Technology
Daejeon 305-701, South Korea
E-mail: linus16@kaist.ac.kr

DOI: 10.1002/adfm.201502751

$$2CO_2 + 8H^+ + 8e^- \rightarrow CH_3COOH + H_2O - 0.29 \text{ versus NHE} \quad (6)$$

$$2CO_2 + 12H^+ + 12e^- \rightarrow C_2H_5OH + 3H_2O - 0.33 \text{ versus NHE} \quad (7)$$

In terms of kinetics, CO_2 reduction reaction is much more complex than the hydrogen evolution reaction (HER) and the oxygen evolution reaction (OER). Unlike water, CO_2 has a linear structure and substantial energy input is required to activate CO_2 to its radical form (CO_2•).[20] As shown in Equations (1)–(7), multiple electron and proton coupling steps are involved in the reaction pathways. The low solubility of CO_2 in water and other organic solvents also makes the reaction difficult.[21,22] Additionally, the thermodynamic energies required for each of the competing reactions, including HER, are so closely distributed that obtaining high chemical selectivity is rarely possible.[11,12,23–25] Apart from those restrictive conditions, the conversion of CO_2 into CO is a relatively simple reaction as it is more favorable than the formation of other hydrocarbons. This is because the former process requires two electrons and protons, as does the formation of H_2. The combination of H_2 and CO, which is referred to as syngas, is also a raw material for liquid fuel and chemical commodities converted via the Fischer–Tropsch reaction.[26]

An attractive strategy, which not only enhances the conversion efficiency for CO but also lowers the cost is to employ a photoelectrochemical process integrated with an electrocatalyst composed of earth-abundant materials. Moreover, this also allows alternative approaches for the conversion of renewable energy into chemical fuel. Silicon (Si) is one of the most earth-abundant elements and has a narrow band gap (≈1.12 eV) suitable for the absorption of a significant portion of the solar spectrum.[27,28] p-Type Si is also proven as an effective photocathode for splitting of water into hydrogen, being fabricated into nanowire.[28,29] Despite its compatibility with already developed processes and its precise controllability, there are few reports on Si-based photocatalytic CO_2 reduction because of its innate poor selectivity for CO (≈75% in organic solvent) and HCOOH (≈20% in aqueous solution).[30,31] In an attempt to enhance the chemical selectivity of p-type Si, various catalysts have been deposited onto the electrode. $[(Me_6\ [14]dieneN_4)\text{-}Ni(II)]^{2+}$ ($Me_6[14]dieneN_4$ = 5,7,7,12,14,14-hexamethyl-1,4,8,11-tetra-azacyclotetradeca-4,11-diene), a molecular catalyst, has been introduced on p-type Si in 1:1 solution of acetonitrile and water. In that reaction, CO and H_2 were produced in a ratio of 1:2 with a faradaic efficiency of 95%,[32] while nearly 100% of faradaic efficiency for CO was achieved in a solution of $Re(bipy\text{-}Bu^t)(CO)_3Cl$ (bipy = 2,2′-bipyridine) dissolved in acetonitrile.[15] However, there have been only a few studies that have employed p-type Si based heterogeneous catalyst for the conversion of CO_2 to CO. The only examples of such catalysts are photodeposited nanoparticles such as Au and Ag on p-type Si, which have been examined in aqueous solution.[33,34] With the expected shift of the *J–E* curve, at most 62% and 50% of CO was evolved for Au and Ag deposited on p-type Si as their bulk states does.[33] Moreover, such photodepositied metals can decrease the surface area of the photocathode. It has been reported that photoeffect of p-type Si was decreased when Cu was overdeposited in the form of a continuous metal layer.[33] Although intensive research has been focused on the selective production of CO from CO_2, there have been few studies on CO_2 reduction using nonmetallic catalysts that have resulted in satisfactory selectivity.[18,35] In addition, the integration of nonmetallic catalyst onto solar powered devices for the selective reduction of CO_2 to CO has not been addressed.

A few studies have shown that the nanostructure of materials can also affect their chemical selectivity for CO_2 reduction. Recently, by preparing bulk Ag as a nanofoam, the chemical selectivity of Ag for CO was enhanced up to 92% at a moderate overpotential of less than 500 mV, which is over three orders of magnitude higher than that of polycrystalline Ag.[5] By introducing microsized pores, a Cu electrode also exhibits entirely different trends in chemical selectivity. In particular, the selectivity toward HCOOH was increased to 37%, compared with smoothly electropolished Cu.[36,37] These dramatic changes in chemical selectivity are thought to originate from the increase in surface area and difference in local crystal structure of the material that resulted from the fabrication procedure.[36,38] However, according to a previous study, the nanowire fabrication of p-type Si is only expected to reduce the onset potential of the catalytic reaction without influencing the chemical selectivity. More recently, the faradaic efficiencies for formic acid on bare planar p-type Si and p-type Si nanowire in aqueous solution were reported to be similarly in the range of less than 10% without help of Sn catalyst.[21]

In addition, due to the low solubility of CO_2 and the prevalent evolution of hydrogen in aqueous solution, nonaqueous based CO_2 reduction has received much attention as a potential alternative. In particular, acetonitrile, which has approximately eightfold higher solubility in CO_2 (270×10^{-3} M) than water (33×10^{-3} M), is considered to be proper solvent for CO_2 reduction.[22] However, even in organic solvents, efficient conversion of CO_2 to CO has been rarely achieved without the help of an active catalyst. It is known that most metal electrodes can be poisoned with CO,[39] resulting in low Faradaic efficiency, and chemisorbed CO_2 intermediates can also form oxalates. Although organic solvents can provide a favorable route for CO_2 reduction, catalysts with a moderate binding energy for CO are the most essential requirement. Moreover, it is also reported that not only solubility of CO_2 but also proton concentration directly affects CO_2 reduction reaction as shown in the Equation (1).[15] Because ideal organic solvent includes no proton in it, hydrogen termination (H-termination) is introduced on the p-type Si photoelectrode to facilitate CO_2 reduction reaction.

Among the homogenous catalysts, Re- or Rh-based molecular catalysts have thus far exhibited the most outstanding performance for CO_2 reduction.[15,40] Generally, these catalysts are photoactive and primarily produce CO with a high chemical selectivity when combined with a photosensitizer. By controlling the organic ligands of the catalyst, their catalytic activity can be further enhanced. In contrast, bulk metal electrodes such as Au and Ag serve as efficient heterogeneous catalysts for CO production.[41,42] The catalytic activities of these catalysts can be increased by fabricating them into nanostructures or by annealing the electrodes in an oxygen environment to convert them into a metal oxide.[41,43] InP and CdTe also have been addressed as possible candidates as CO-producing heterogeneous photocathodes.[30,44] Recently, by introducing N

into carbon nanofibers, enhanced catalytic activity for CO evolution has been reported.[18,35,45–49] However, it has not been proven for reducing CO_2 using carbon material, integrated on photoelectrode.

Herein, we describe the development of nitrogen-doped graphene quantum sheets (N-GQSs) for catalyzing the selective photoreduction of CO_2 into CO on p-type Si nanowire. The reduction of CO_2 into CO on our catalyst exhibited enhanced current density with an onset potential much lower than that required for photodeposited Cu on a p-type Si electrode. To verify the source of the evolved CO, an isotope tracing experiment using $^{13}CO_2$ gas was conducted. Using density functional theory (DFT) calculations, we investigated the band alignment between p-type Si and N-GQSs to understand the electron transfer pathways taking place. We then proposed a plausible CO_2 to CO reduction mechanism based on the DFT binding energies of possible intermediates.

2. Result and Discussion

To evaluate the effect of the nanowire structure on the photocathodic behavior, cyclic voltammetry measurements for planar p-type Si and p-type Si nanowire with etching times of 10, 20, 30, 40, 50, and 60 min in a CO_2 environment without N-GQSs were performed in light condition (**Figure 1**a). To compare the catalytic activity of each electrode, the potential required to achieve a catalytic current density of 0.15 mA cm^{-2} was defined as the onset potential. As shown in Figure 1b, on planar p-type Si without N-GQSs, the current density increased gradually from –2.1 V versus Ag/Ag^+ and reached 0.51 mA cm^{-2} at –2.5 V versus Ag/Ag^+ as the potential was negatively applied. The length of the nanostructures ranging from 1 to 12 µm, as confirmed by SEM (Figure S1a–f, in the Supporting Information) strongly affects the photoelectrochemical performance of the Si electrodes; the p-type Si nanowire electrodes exhibited the lowest onset potential and the highest current density when the length of the nanowires was 8 µm. However, the 60 min etched Si nanowire with a length of 12 µm exhibited a negative shift of the *J–E* curve by ≈100 mV more than that of the 50 min etched Si nanowire. In general, the overpotential of a photocathode can be lowered by increasing its surface area and light adsorption. By fabricating nanowires, the Si electrodes have an increased surface area compared with the planar structure, thus providing more reaction sites.[50] The photon absorption also increases for the nanostructured surface due to the low reflectance, while the surface of planar Si reflects about a quarter of the incident light.[50–53] A possible explanation for the decrease in current density for the 60 min etched Si nanowire is the presence of surface traps or defect sites, which have more chances to be generated in longer nanowires. Based on these results, the 50 min etched p-type Si with a length of 8 µm was found to be optimal for facilitating the catalytic reduction of CO_2.

The photoelectrochemical performances of N-GQSs on p-type Si were measured by cyclic voltammetry. The photoresponse of N-GQSs on p-type Si nanowire was measured separately under chopped irradiation (Figure S2, Supporting Information). To compare their photocatalytic behaviors, two parameters, the onset potential to achieve 0.15 mA cm^{-2} and the current density recorded at –2.5 V versus Ag/Ag^+, were chosen as figures of merit. The values for each photocathode are organized in **Table 1**. As shown, for planar p-type Si with N-GQSs, the required photocurrent of 0.15 mA cm^{-2} is observed at –1.78 V versus Ag/Ag^+ and then increases to 4.89 mA cm^{-2} at –2.5 V versus Ag/Ag^+, which is approximately nine times higher than that of planar p-type Si without N-GQSs. The onset potential is positively shifted by 450 mV compared with that of planar p-type Si. Further enhancement in both the onset potential and current density were achieved

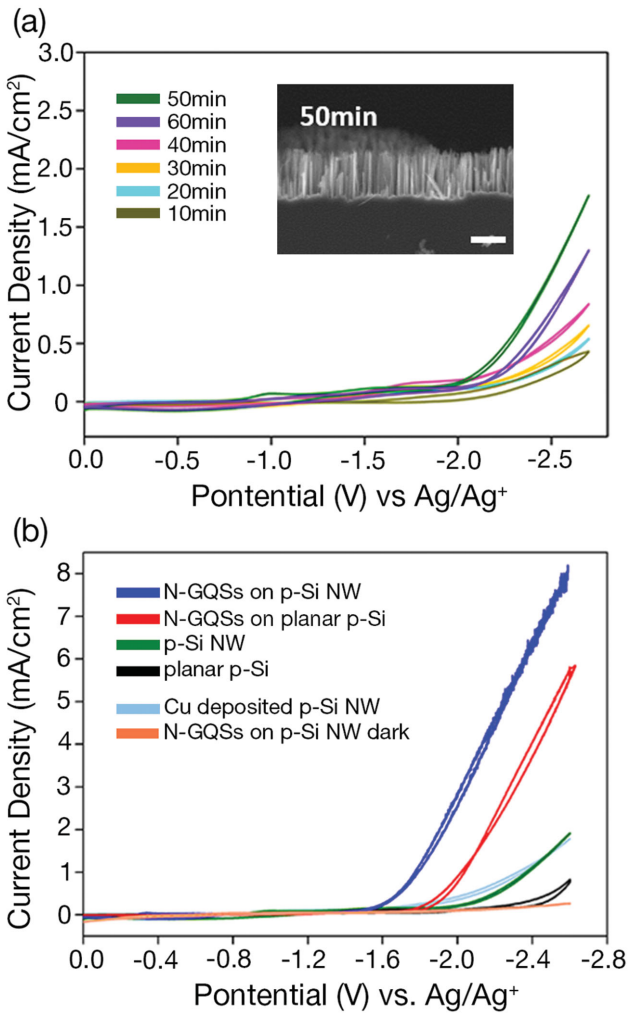

Figure 1. a) Cyclic voltammetry curves of p-type Si nanowire produced with etching times of 10 min (olive), 20 min (cyan blue), 30 min (light orange), 40 min (pink), 50 min (purple), and 60 min (green) under light. A cross-sectional SEM image of p-type Si etched for 50 min is shown in the inset (scale bar = 5 µm). b) Photocurrent density–potential (*J–E*) curve of N-GQSs on p-type Si nanowire (blue) compared with those of N-GQSs on planar p-type Si (red), p-type Si nanowire (green), planar p-type Si (black), photodeposited Cu on p-type Si NW (dashed, light blue), and dark current of N-GQSs on p-type Si nanowire (dashed, orange). A cyclic voltammetry measurement was conducted in acetonitrile with 100 mM TBAH at a scan rate of 100 mV s^{-1}. Limiting current density is not depicted because the measurement was conducted within the electrochemical window of acetonitrile. The current values were normalized by the surface area of the electrodes.

Table 1. Performances of various p-type Si based photoelectrodes for the photoelectrochemical reduction of CO_2.

Catalyst	Onset potential [V vs Ag/Ag^+]	Current density [mA cm^{-2}] @ −2.5 V versus Ag/Ag^+
N-GQSs on p-type Si NW	−1.53	7.07
N-GQSs on planar p-type Si	−1.78	4.89
p-Type Si NW	−1.9	1.49
Planar p-type Si	−2.1	0.51
Cu deposited p-type Si NW	−1.66	1.47

by fabricating the Si substrate into the nanowires. The cyclic voltammogram of the N-GQSs on the p-type Si nanowire surfaces exhibits spikiness at highly negative potentials due to the sudden bursting of bubbles of reduced product that stuck to the Si surfaces. The overall *J–E* curve is shifted by ≈200 mV toward positive potentials compared with N-GQSs on planar p-type Si. The current density of the N-GQSs on p-type Si nanowire increased gradually from the onset potential of −1.53 V versus Ag/Ag^+ and reached 7 mA cm^{-2} at −2.5 V versus Ag/Ag^+. This value is approximately five times higher than that of p-type Si nanowire without N-GQSs. Two reductions are observed from the cyclic voltammograms, which is similar to the results of previous studies (Figure S1g, Supporting Information).[15] At the first reduction, the current density increases to 0.03 mA cm^{-2} at an applied voltage of ≈−0.9 V versus Ag/Ag^+. Then, the photocurrent exhibits the second reduction under a CO_2 environment, providing a current density of more than 0.15 mA cm^{-2}. It is known that this behavior implies the catalytic conversion of CO_2 to CO because the reaction requires a doubly reduced catalyst, as shown in Equation (1).[15] Indeed, the shift of second reduction can be observed when the photoelectrode is not hydrogen terminated (H-termination) as shown in Figure S7 (Supporting Information). Because proton directly participates CO_2 reduction reaction, ≈0.4 V shifted second reduction in H-terminated p-Si means this originated from catalytic reaction. In addition, there was no increase in the second reduction under an Ar environment. Therefore, the positive shift in the onset potential and the increased current density at −2.5 V versus Ag/Ag^+ on the p-type Si photocathode with N-GQSs directly indicate that N-GQSs enhance the catalytic reduction of CO_2.

Taken together with the nanostructure effect and catalytic activity of N-GQSs, the catalytic performance of N-GQSs on p-type Si nanowire was compared with previously reported catalysts. For instance, $Re(bipy\text{-}Bu^t)(CO)^3Cl$ is known to exhibit the second reduction at −1.23 V versus the Ag/AgCl pseudo reference electrode on a p-type Si photocathode.[15] This potential corresponds to −1.55 V versus Ag/Ag^+, which is cathodically shifted by 20 mV compared with that of N-GQSs on p-type Si nanowire. Photodeposited Cu on p-type Si nanowire, which is a well-known metal catalyst for solar-driven CO_2 reduction, was also prepared for comparison. This electrode exhibits an onset potential of −1.66 V versus Ag/Ag^+, which is negatively shifted by 130 mV compared with N-GQSs on p-type Si nanowire, respectively.[33] Still, N-GQSs on p-type Si is approximately five-fold more active at 2.5 V versus Ag/Ag^+. Moreover, in order to confirm whether the N-GQSs is poisoned with CO or not, linear sweep voltammetry was conducted under CO_2 and CO environment. Voltammograms of N-GQSs on planer p-type Si in CO_2 environment were identical before and after performing the same measurement in the CO atmosphere (Figure S3, Supporting Information), demonstrating the catalyst is not poisoned with CO during CO_2 reducing reaction. Therefore, compared with previously reported homogenous and heterogeneous catalysts, N-GQSs on p-type Si nanowire exhibit superior catalytic activity in terms of both onset potential and current density.

The N-GQSs on p-type Si nanowire produced CO with a remarkably high efficiency of 95%, which is the highest value achieved by a Si-based heterogeneous CO_2-reducing catalyst in organic solution. To date, polyaniline-coated p-type Si has been the only example of a catalyst providing metal-free Si-based CO_2 reduction; however, it produced formate with a low selectivity of 21.2%.[31] In the gas chromatograms for products evolved in the second reduction region, CO and H_2 were detected as the main products. In **Figure 2**a, the Faradaic efficiencies of CO are plotted against the applied voltage to determine trends in the input energy dependence of the efficiencies. Approximately 75% of the electrons are reported to be consumed for reducing CO_2 into CO on bare planar p-type Si electrodes.[30] However, by decorating N-GQSs on planar p-type Si, the chemical selectivity for CO is dramatically enhanced by 15%. More interestingly, when the Si substrate is fabricated into nanowires, CO is more exclusively evolved with a selectivity of up to 95%. It is notable that this high faradaic efficiency for CO was maintained with a negligible deviation (±3%) throughout the range of applied potentials, from −1.9 to −2.5 V versus Ag/Ag^+. In typical cases, it is known that the faradaic efficiency for CO has an optimal potential ranges. [54] Therefore, the observed wide maintenance of the efficiency demonstrates that CO evolves very stably on p-type Si nanowire with N-GQSs in wide ranges of the applied potential once the CO_2 molecule is activated. Meanwhile, the faradaic efficiency corresponding to H_2 was 2% (±1%) and the sum of the faradaic efficiencies for CO and H_2 was nearly 100%. To verify the rest of the faradaic efficiencies, high performance liquid chromatography (HPLC) was conducted using a UV–vis diode array detector. However, no other compounds, including the prime suspect, oxalate, which can be synthesized by the coordination between two adsorbed CO_2 molecules, were detected. The remaining 2% efficiency can be attributed to the dissolution of CO in acetonitrile or the reoxidized of oxalate on the anode.

To confirm the accuracy of the observed faradic efficiency and the stability of the catalyst, the number of moles of electrons was plotted against the amount of evolved of CO. The diagram contains values corresponding to N-GQSs on p-type Si nanowire, bare p-type Si, and an ideal CO-producing catalyst, and the electrolysis was conducted at moderate voltage of −2.1 V versus Ag/Ag^+.[30] As shown in Figure 2b, a linear relationship was observed between the number of moles of CO and the number of moles of electrons. Because faradaic efficiency is derived from the ratio of moles of electrons to moles of evolved products compared with the stoichiometric calculation (100%), the slope of the diagram is directly related to the columbic efficiency. The number of moles of electrons exhibited a linear relationship with the amount of CO produced, with

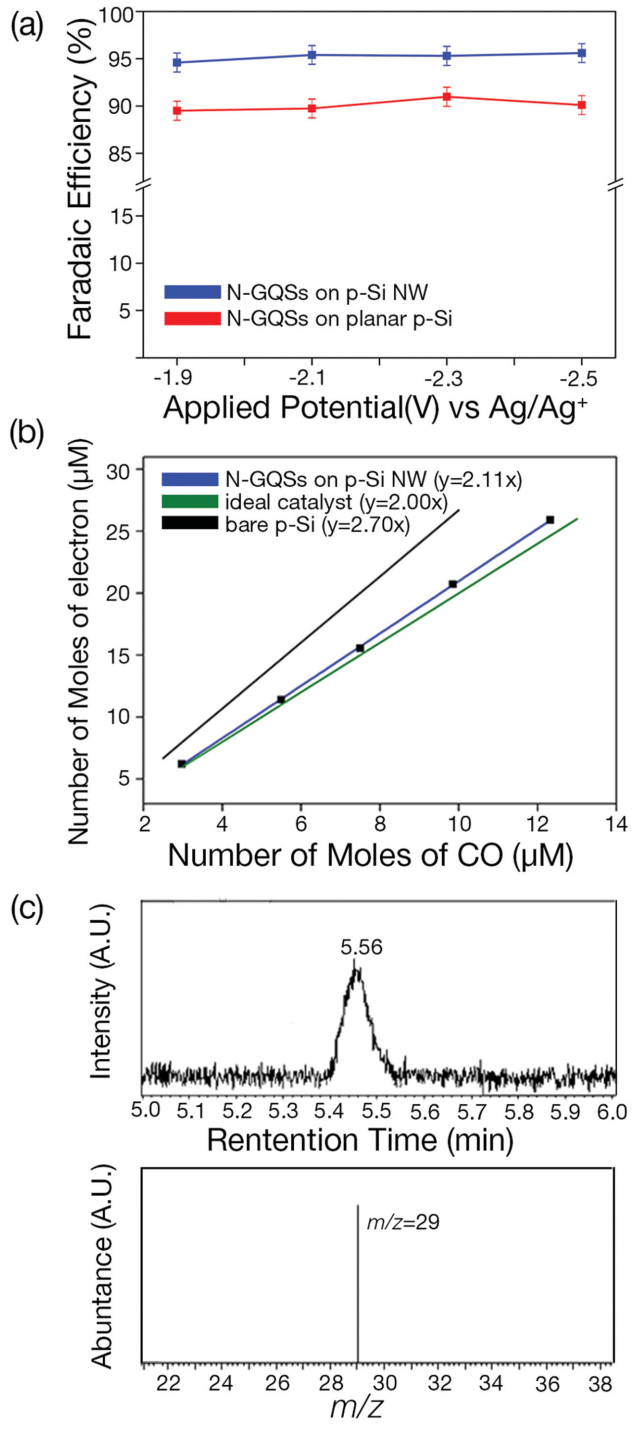

Figure 2. a) Faradaic efficiencies of CO on p-type Si nanowire with N-GQSs at various potentials: –1.9, –2.1, –2.3, and –2.5 V versus Ag/Ag+. b) Relationship between the number of moles of electrons consumed and the number of moles of CO produced as a result of bulk electrolysis under a CO_2 environment at –2.1 V versus Ag/Ag+ and under illumination. The inverse value of the slope of the graph divided by 2, i.e., the number of electrons required to produce CO from CO_2, corresponds to the faradaic efficiency (%). The standard deviation of the slope corresponding to N-GQSs on p-type Si is 0.01. The slope of bare p-type Si was calculated from a reference paper. c) Gas chromatogram of CO and mass spectra after 3 h of photocatalytic conversion of $^{13}CO_2$. The peak at $m/z = 29$ corresponds to ^{13}CO.

a slope of 2.11 and standard deviation of 0.01. This corresponds to a faradaic efficiency of 95% (±1). While the bare p-type Si exhibited a steep slope ($y = 2.70x$), which corresponds to ≈75% selectivity, N-GQSs on p-type Si shows a very similar value to that of an ideal catalyst ($y = 2.00x$). This linearity and similarity of the slope to the ideal value further support the fact that the N-GQSs on p-type Si nanowire catalyst is highly stable and selective for the photoreduction of CO_2 to CO, within a negligibly small error.

Furthermore, to verify that the evolved CO did not originate from remaining carbon residue, electrolysis was performed using ^{13}C labeled CO_2 as a reactant. In the gas chromatogram, using $^{12}CO_2$ as a control experiment, a peak for CO was observed at 330 s. When the mass spectrum of this peak was analyzed, a signal at $m/z = 28$ was observed, which corresponds to ^{12}CO (Figure S4c, Supporting Information). When the same experiment was conducted for $^{13}CO_2$-purged acetonitrile, a peak was observed at the same retention time of 330 s; however, only a signal at $m/z = 29$ appeared in the mass spectrum for this peak. This is direct evidence that the evolved CO originates solely from $^{13}CO_2$ gas and not from the reduction of carbon residue or the decomposition of N-GQSs.

Measurements of the photoelectrochemical performance in a CO_2 environment show that N-GQSs on p-type Si exhibits catalytic CO_2 reduction activity. In the cyclic voltammetry analysis, the onset potential was –1.53 V versus Ag/Ag^+, and the current density was also enhanced, reaching 7.07 mA cm^{-2} at –2.5 V versus Ag/Ag^+. The onset potential is 20 mV lower than that of a Re-based homogeneous catalyst, and the current density was also enhanced fivefold compared with that of photodeposited Cu on p-type Si nanowire. Even in the GC analysis, the Si photocathode decorated with N-GQSs exclusively produced CO with a faradaic efficiency of over 95%. It is worth noting that the photoconversion of CO_2 into CO with a faradaic efficiency of over 80% has not been previously reported in a heterogeneous system. Moreover, the selective conversion of CO without the use of a noble metal is critical with regard to cost. To elucidate the origin of the enhancement of the catalytic activity by N-GQSs, an investigation of the chemical states of the catalyst was carried out using Raman spectroscopy, XPS, and HRTEM. Based on these observations, the role of doped nitrogen in GQSs on the catalytic reduction of CO_2 as well as the catalytic mechanism were subsequently investigated using computational simulations on different sized N-GQSs on p-type Si.

The changes in the chemical states of N-GQSs after nitrogen doping are depicted in **Figure 3**. The Raman spectrum of a solution of GOs and N-GQSs exhibits the characteristic D peak related to structural defects. The peaks centered at ≈1360 cm^{-1} and ≈1580 cm^{-1} are the typical D and G bands, respectively, of carbon materials. The G peak of N-GQSs (1600.93 cm^{-1}) is blueshifted with respect to that of the original GO (1596.64 cm^{-1}), suggesting that the intercalation of N atoms into the conjugated carbon backbone leads to disordered structures.[55] As in the case of GO and graphite, the Raman G peak of GO is blueshifted from that of graphite (1580 cm^{-1}), presumably because the defect structures introduces isolated double bonds, which resonate at higher frequencies. The D peak is observed due to the breathing modes of six-atom rings, which originate from transverse optical phonons around the

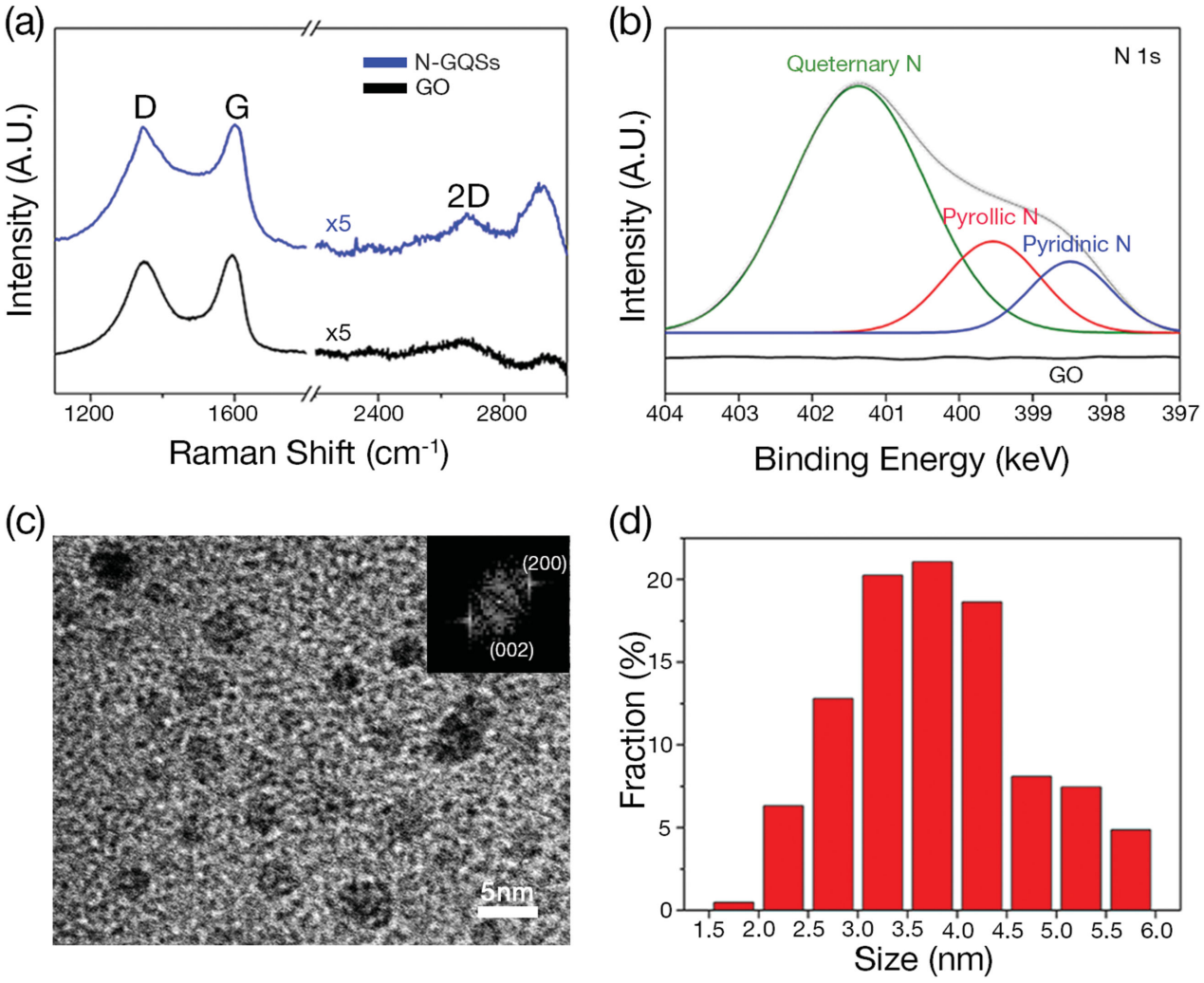

Figure 3. a) Raman spectra of GO (black) and N-GQSs (blue) and b) XPS spectra of N-GQSs. The N 1s peak is separated into pyridinic N (398.5 eV), pyrrolic N (399.7 eV), and quaternary N (401.2 eV), which are labeled by blue, red, and green lines, respectively. Narrow-scan data were collected using a pass energy of 23.5 eV and 0.05 eV per step. The N-GQSs consist of 2 at% of N. c) TEM image of N-GQSs on monolayer graphene supported by holey carbon grids. d) Corresponding size distribution graph, which shows that the average size of the N-GQSs is 3.62 nm (±0.27 nm).

K or K′ point in the first Brillouin zone. Because the D peak reflects the existence of defects in graphene, the intensity ratio of the D peak to the G peak (I_D/I_G) is a measure of the disorder. Tuinstra-Koening has suggested on an empirical basis that the distance between defects (L_d) is proportional to $(I_D/I_G)^{-1/2}$, on account of the presence of point-like defects in graphene.[56] It was observed that the N-GQSs has an I_D/I_G ratio of 0.93, which is much lower than that of the original GO (1.02). Therefore, the heteroatom N dopants cause a decrease in L_d by disrupting the conjugated sp^2 cluster and increasing the point-like defect density through the generation of disordered structures. Moreover, the D + G combination peak at 2950 cm^{-1} requires defects for its activation.[57] Atomic force microscopy (AFM) was performed to examine the change in local structure of the N-GQSs topographically. The AFM images reveal that plenty of edges were generated on the surface of the N-GQSs, while that of GO is smooth (Figure S5, Supporting Information).

X-ray photoelectron spectroscopy (XPS) was performed to determine the change in chemical composition induced by the N-doping of the as-produced N-GQSs. The XPS survey spectra of the starting material, GO, and the resultant N-GQSs are shown in Figure 3b. The spectra exhibit a predominant graphitic C 1s peak at 284 eV and an O 1s peak at 532 eV, with an O/C ratio of 64.9%. This ratio indicates that O-rich groups in GO, which tend to be removed, are restored due to accelerated intramolecular and intermolecular dehydration during the hydrothermal reaction. A pronounced N 1s peak was also observed for the resultant N-GQSs with a concentration of ≈3.5 at%, whereas no N signal was detected for the GO (Figure S5, Supporting Information). The N 1s peak of the N-GQSs can be deconvoluted into signals for pyridinic N (398.5 eV), pyrrolic N (399.9 eV), and quaternary N (401 eV), all of which agree with their previously assigned peak positions. The quantitative analyses demonstrate that the fraction of the various nitrogen

species is ≈12.95% for pyridinic N, 21.54% for pyrrolic N, and 65.4% for quaternary N.

The N-GQSs were also observed using high-resolution transmission electron microscopy (HRTEM). The sample was prepared by drop-casting the N-GQSs solution on a monolayer graphene-supported holey carbon grid. The TEM images revealed fairly uniform N-GQSs with diameters of 2–6 nm and an average value of 3.62 nm (±0.27 nm), as shown in Figure 3d. The clear atomic lattice structure indicates that the N-GQSs are highly crystalline (Figure S1d, Supporting Information). The Fast Fourier Transform (FFT) image of the catalysts shows that the local structure of the surface resembles that of the graphitic materials, with *d* spacing values of 0.28 and 0.32. These are close to the values of the (020) and (002) planes of graphitic carbon, respectively, confirming the graphitic nature of the N-GQSs.[58–60] Moreover, these observations are quite consistent with the AFM measurements for the corresponding N-GQSs. Most of the N-GQSs have an average height of 2.5–5 nm (Figure S1a,b, Supporting Information).

A more profound understanding of the mechanism of selective CO_2 to CO conversion was provided by DFT calculations. As the first step, the band edge position of GQS was considered with regard to band alignment with p-type Si. Interestingly, the size of the GQS significantly affects their electron affinity and band alignment. The calculated band edge positions of various sizes of GQS ranging in diameter from 0.96 nm ($C_{24}H_{12}$) to 3.4 nm ($C_{294}H_{42}$) with respect to the experimental conduction band of p-type Si is shown in **Figure 4**a. The position of the conduction band minimum (ϵ_{CBM}) of GQS decreases as the diameter was increased until ≈3 nm and is eventually located more negative than that of p-type Si when the diameter becomes larger than 3 nm. Therefore, the photoexcited electrons in p-type Si can be transferred to the GQS and participate in the catalytic reduction of CO_2 when the diameter is larger than 3 nm. It should be noted that the average size of the N-GQSs is 3.62 nm, as determined by HRTEM. Moreover, the effect of N dopants on the value of ϵ_{CBM} was further investigated, as shown in Figures S10 and S11 (Supporting Information). For the smallest GQS, doping with pyrrolic N raises ϵ_{CBM} by 0.14 V, while doping with pyridinic N and quaternary N on edge sites lowers (or does not change) ϵ_{CBM}. Indeed, the XPS and Raman spectra indicate the formation of abundant defect sites in the N-GQSs primarily at quaternary N and pyridinic N positions; N-doping at these two types of sites accounts for ≈90% of the total. Together, these nitrogen dopants in N-GQSs are expected to help lower the value of ϵ_{CBM} in the actual experimental samples, which results in the enhancement of the electrocatalytic activity for CO_2 reduction. However, it should be noted that the major effect in determining the band edge positions is the size of the N-GQSs, while the effect of N dopants is minor.

After the excited electron from the CB of p-type Si is transferred to N-GQSs, the negatively charged N-GQSs are required to bind CO_2 for its reduction. To verify the exact active site, calculation of CO_2 binding energies to four different N-doped sites were followed as shown in Figure 4b and Figure S10 (Supporting Information). Among different possible active sites, only pyridinic N showed a substantial binding energy of 0.37 eV, making complex with the CO_2 molecule. The lone pair of pyridinic group attacks the electrophilic carbon atom of the CO_2 molecule, forming a C–N single bond while breaking one of the double bonds of CO_2. The change of sp to sp^2 hybridization accompanies bending of the linear CO_2 molecule from 180° to 130°, and thus the pyridinic site is turned out to serve as an active center. This provides a clue to understand the observation from the GC analysis conducted for various applied potential (Figure 2a). In the measurement, N-GQSs decorated p-type Si stably produces CO regardless of the intensity of applied voltages. Taken together, pyridinic N sites in N-GQSs offer favorable binding sites to activate CO_2 and facilitate its catalytic reduction.

Based on the results of the DFT calculations, the overall photoelectrocatalytic reduction mechanism of CO_2 to CO is summarized in **Figure 5**. The steps involved are (1) the first

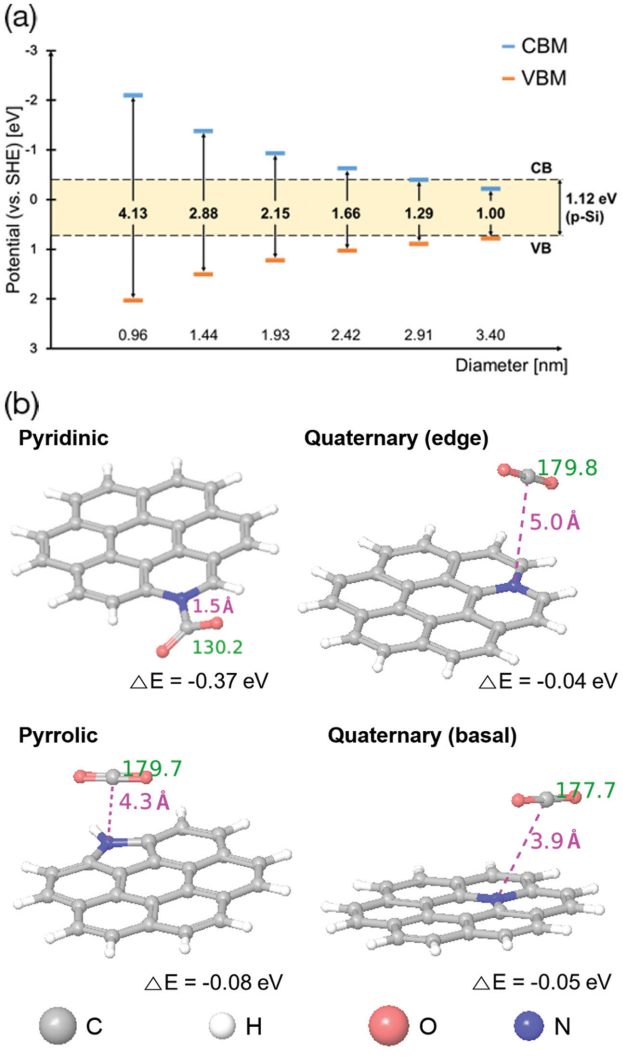

Figure 4. a) Band alignment of p-type Si and calculated band edge positions of different sized GQS. The level of the CB edge decreases with increasing GQS diameter. If the diameter is >3 nm, the CB edge is more negative than that of p-type Si, resulting in electron transfer from p-type Si into GQS. b) Optimized structures of four different -1 charged N-GQS-CO_2 complexes. The values of the binding distance between N and CO_2 (magenta color) and O–C–O angle (green color) are displayed.

N-GQS reduction, (2) adsorption of CO_2 to the pyridinic N site, (3) the first protonation, (4) the second N-GQS reduction, and (5) the second protonation to yield CO and H_2O. The DFT calculations show that the first and second protonation steps are also energetically downhill by 1.07 and 2.76 eV, respectively. In conjunction with the aforementioned results showing the energetic feasibility of N-GQSs reduction and CO_2 adsorption, all of the elementary reaction steps of the catalytic cycle become energetically favorable. In these calculations, the absolute proton solvation free energy in acetonitrile, –11.28 eV, was employed to compute the energetics for the protonation steps.[61]

3. Conclusions

We have successfully demonstrated the selective photoconversion of CO_2 into CO on p-type Si nanowire with N-GQSs in acetonitrile. The second reduction of our N-GQSs on p-type Si nanowire, which is directly related to the CO_2 reduction, occurred at –1.53 V versus Ag/Ag^+. The performance is superior to that of Re-containing catalysts, which had previously provided the best catalytic activity in nonaqueous solution. In the first demonstrated application of N-GQSs as a heterogeneous electrocatalyst on p-type Si nanowire, the chemical selectivity for CO was enhanced with a faradaic efficiency of more than 95%. By measuring the amount of gas produced against the number of coulombs of electron passed, we have also verified the stability of our catalyst. Additionally, the isotope tracing performed with $^{13}CO_2$ successfully verified that our N-GQSs did not decompose during electrolysis and that carbon residues do not contribute to the CO conversion. The performed DFT calculations provided an atomistic level of understanding of the reaction mechanism. The results suggest that N-GQSs larger than 3 nm can efficiently take electrons from the conduction band of p-type Si. Among the various possible types of N-doping sites, pyridinic N lowers the binding energy for CO_2 the most and is considered to be the primary active site of the studied system. Based on these results, we have proposed an overall photoelectrocatalytic mechanism. We expect that our studies on this metal-free catalyst will provide valuable insight for the design of other new metal-free CO_2 reduction systems.

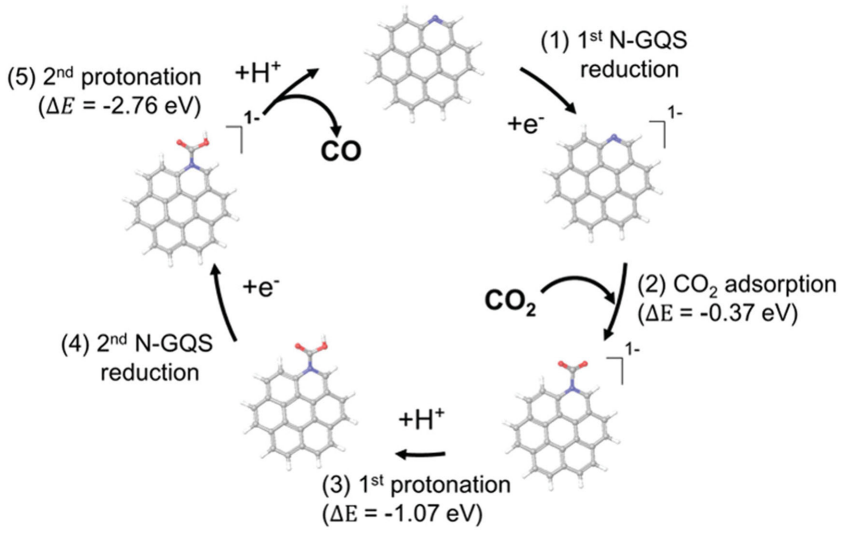

Figure 5. Proposed photoelectrocatalytic cycle of CO_2 to CO reduction on pyridinic N doped coronene ($C_{24}H_{12}$).

4. Experimental Section

Sample Preparation—Synthesis of N-GQSs: N-GQSs were synthesized by the previously reported hydrothermal method.[62] 70 mg of graphene oxide powder was dispersed in 30 wt% ammonium hydroxide. The solution was diluted by 18.2 Mohm Millipore water to reach 2.5 mol L^{-1} in 70 mL. The resulting brown dark solution was then followed by ultrasonication for 1 h to ensure its homogeneity. After transferred into Teflon-line Stainless-steel autoclave, the reactor was heated at 230 °C for 14 h. Through this solvothermal treatment, nitrogen doping was conducted. After cooling down to room temperature, the desired N-GQSs at the supernatant were centrifuged at 15 000 rpm for 30 min to remove the rest of unreacted GO. The supernatant was naturalized by hydrochloric acid and condensed by a rotating evaporator. Carefully transferred into tubing bag with 2000 Da of molecular weight cut off, the desired N-GQSs solution was dialyzed for 1 d to remove salts from ammonium hydroxide and hydrochloric acid. The N-GQSs then transferred to p-type Si by drop casting.

Sample Preparation—Si Nanowire Fabrication and Ohmic Contact Establishment: After being cut into 8 × 8 mm^2 pieces Boron-doped (p-type) single crystal Si wafers (4 in. diameter, 500 mm thickness, normal doped with 10–15 Ω cm, (100) oriented, Namkang Co. Ltd.) were cleaned in acetone, 2-propanol and deionized water for 10 min, respectively, by sonication. The Ag-catalyzed electroless chemical etching of the p-type Si wafer in 20 mL aqueous solution of $AgNO_3$ (0.679 g, 0.02 M) and HF (5 M) produced vertically aligned, free-standing Si wires on the substrate. Excess Ag residues were completely washed with 70% nitric acid solution for 2 h and rinsed in deionized water. Ohmic contact was established between copper wire and the unpolished side of the Si wafer embedded in high-purity liquid metal alloy of gallium-indium (Kojundo Chemical). Additionally, epoxy (Loctite Hysol 9460) was used to insulate and protect the back contact between p-type Si and Cu wire. All electrodes were hydrogen terminated (H-terminated) before cyclic voltammetry and gas chromatography measurement in 40 wt% NH4F solution under argon for 20 min to enhance catalytic property of the electrode.

Sample Preparation—Photodeposition of Cu on p-Type Si Nanowire: Electrodeposition was conducted on 50 min etched p-type Si nanowire electrode in the solution of 0.01 M $CuSO_4$ and 0.18 M H_2SO_4 using Pt foil as a counter electrode. Charge was accumulated up to 160 mC at constant applied voltage of –0.1 V, illuminated by 100 mW Xe lamp while conducting bulk electrolysis (Figure S7b, Supporting Information). The Cu deposited p-type Si nanowire was electrochemically etched in 70% phosphoric acid at 0.1 V versus Ag/AgCl to remove surface oxide layer of Cu before cyclic voltammetry measurement.

Characterization of N-GQSs—Raman Spectra and XPS Analysis: Raman spectra were obtained with confocal Raman microscope (WiTec Alpha300) using 532 nm excitation source from a frequency-doubled Nd:Yag laser. The spot diameter was ≈2 mm with an objective lens multiplied by 50 times. X-ray photo-electron spectroscopy (XPS) spectra were obtained by electron spectroscopy (PHI 5000 VersaProbeTM, ULVAC-PHI) with a pass

energy of 23.5 eV and a step size of 0.05 eV. All the binding energies are referenced to C 1s (284.5 eV).

Characterization of N-GQSs—HR-TEM Analysis: High resolution TEM images and fast Furier transformation (FFT) patterns were obtained using a high resolution transmission electron microscope (JEM-3000F, JEOL, Japan) with an acceleration voltage of 300 kV. The TEM grids were prepared by transferring monolayer graphene on lacey carbon grid. The monolayer graphene was deposited on Cu by chemical vapor deposition (CVD) method without protecting layer such as PMMA. The Cu layer was etched in 0.1 M ammonium persulfate solution. The TEM samples were collected from as-prepared N-GQSs. Approximately 10 µL of dispersed N-GQSs in water was dropped on the graphene supported lacy carbon TEM grid and air-dried. The grids were then further dried in a vacuum oven at 70° for 30 min to evaporate the solvent.

Electrochemical Measurement—Electrochemical Methods: All the electrochemical measurement were performed in a three-electrode electrochemical cell system. A ALS Ag/Ag^+ reference electrode (in 0.1 M tetrabutyl ammonium hexafluorophosphate (TBAH) and 0.01 M $AgNO_3$) and Pt foil (2 cm × 2 cm × 0.1 mm, 99.997% purity, Alfa Aesar) were used as the reference electrode and counter electrode, respectively. The applied potential of p-type Si was controlled using a potentiostat system (CHI 760E, CH Instruments, Inc.) at ambient temperature (21 ± 1 °C). Based on the redox potential of ferrocene, the potential of Ag/Ag^+ reference electrode has a relation with that of Ag/AgCl by following equation: $E(Ag/AgCl/3M\ NaCl) = E(Ag/Ag^+) - 0.4$ V. The electrolyte in all experiments was 0.1 M TBAH in dry acetonitrile unless cited. The electrolyte was degassed by bubbling with high-purity Argon (99.999%) before the start of each experiment then purged with high-purity CO_2 (99.999%) for at least 30 min.

Electrochemical Measurement—Cyclic Voltammetry Measurement: Current density was measured, as the potential sweeping from 0.0 V to −2.6 V versus Ag/Ag^+ using. To avoid decomposition of acetonitrile, ≈1.7 V to −3.1 V versus Ag/Ag^+, the negative potential was not applied more than the electrochemical window of acetonitrile. All cyclic voltammograms were measured at a scan rate of 100 mV s^{-1}. Additionally, iR compensation was performed by following equation ($V = V_{applied}$−iR). A light source of a 300 W Xe lamp was illuminated on the p-type Si photoelectrode, passed by the Air Mass 1.5 Global condition filter. The light intensity was calibrated to be 100 mW cm^{-2}, using Newport 1916-R photo monitor/meter.

Gas Analysis—Gas Chromatography: The products were quantitatively analyzed by flame ionization detector gas chromatography (FID-GC, PerkinElmer, NARL8502 Model 4003) equipped with an active-carbon-packed column (6′ HayeSep N 60/80 SF, carrier gas: Ar) at 120 °C. One milliliter of the gas was injected into the FID-GC by a syringe at the designated time. The molar proportion of the products relatively was measured by FID-GC and the exact amount of gas was calculated by multiplied by the head space of the reactor. The number of moles of CO evolved during electrolysis was calculated from the integrated area of the CO peak in the gas chromatogram using 0.1 mol% of CO as a standard gas. The Faradaic efficiency for the photoreduction of CO_2 was measured by running a controlled potential electrolysis without stirring at a various potential from 300 mV to 1 V more negative than the second reduction using N-GQSs on p-type Si nanowire without iR compensation.

Gas Analysis—Mass Spectrum Analysis for ^{13}CO: A 10 L quantity of isotope $^{13}CO_2$ gas were purchased from Cambridge Isotope Laboratories and directly used. The mass of the products were confirmed by gas chromatography mass spectrum (GC-MS, Agilent, 7890A GC/5977A MS) using a quadrupole-type mass spectrometer and HP-PLOT molesieve capillary column (Agilent). Typically, electrolysis was conducted in $^{13}CO_2$ purged acetonitrile for an hour at −2.1 V versus Ag/Ag^+ and the gas products were carefully transferred to evacuated 20 mL of cramp type headspace vial through a needle. Then 100 µL of the gas was injected into the GC-MS by a syringe. The mass of products were analyzed after segregation by a gas chromatograph.

Computational Details: Density functional theory (DFT) calculations were performed using Jaguar 8.2 program as built in Schrödinger Suite 2013.[63] All geometries were fully optimized using the Becke's three parameter (B3) functional with the Lee-Yang-Parr (LYP) correlation functional (B3LYP)[64] under the Poisson-Boltzmann implicit solvation method (PBF). Dielectric constant and probe radius were set to 37.5 and 2.19 Å, respectively, to account for the solvation effects of acetonitrile.

To examine the catalytic pathways of N-GQSs, an N-doped coronene molecule ($C_{23}NH_{12}$) with a diameter 0.96 nm was employed as a model system of N-GQS under the assumption that the chemical binding energies are mostly determined by the local chemical environment near at the active center. DFT energies were calculated at the higher level of accuracy using large basis set of Pople 6-311G**.[65]

For the investigation of band alignment, various sizes of graphene quantum sheets (GQSs), from the diameter of 0.96 to 3.40 nm, were calculated. For the smallest GQS of $C_{24}H_{12}$ where high-level full calculation is available using large 6-311G** basis set, the conduction band minimum position (ϵ_{CBM}/6-311G**) under solvation effect with respect to the SHE position was defined by computing the standard reduction potential (E_0) of GQS using the Born-Haber cycle shown in Figure S8 (Supporting Information).[66] For larger size of GQS where only low-level calculations are available using small MidiX basis set, the accurate ϵ_{CBM} was estimated by shifting the location of lowest unoccupied molecular or bital (LUMO) from the low level calculation (ϵ_{LUMO}/MidiX) by Δ; $\epsilon_{CBM} = \epsilon_{LUMO}/MidiX - \Delta$. Here the correction term Δ is set by $\epsilon_{0LUMO}/MidiX - e_{0CBM}$/6-311G**, where the zero subscript denotes the values of the smallest GQS ($C_{24}H_{12}$). The valence band maximum position (ϵ_{VBM}) was defined using the band gap of GQS (E_g) computed as the difference of LUMO and HOMO energy levels. $\epsilon_{VBM} = \epsilon_{CBM} - E_g = \epsilon_{CBM} - (\epsilon_{LUMO} - \epsilon_{HOMO})$.

Supporting Information

Supporting Information is available from the Wiley Online Library or from the author.

Acknowledgements

This research was supported by the Basic Science Research Program (2011-0011225), the Global Frontier R&D Program of the Center for Multiscale Energy System (0420-20130104), and the Fusion Research Program for Green Technologies (2012M3C1A1048863) through the National Research Foundation of Korea funded by the Ministry of Science, ICT & Future.

Note: Figure 3 was amended on January 13, 2016.

Received: July 6, 2015
Revised: September 3, 2015
Published online: December 2, 2015

[1] Y. Jiao, Y. Zheng, M. Jaroniec, S. Z. Qiao, *Chem. Soc. Rev.* **2015**, *44*, 2060.
[2] F. Studt, I. Sharafutdinov, F. Abild-Pedersen, C. F. Elkjær, J. S. Hummelshøj, S. Dahl, I. Chorkendorff, J. K. Nørskov, *Nat. Chem.* **2014**, *6*, 320.
[3] A. A. Peterson, J. K. Nørskov, *J. Phys. Chem. Lett.* **2012**, *3*, 251.
[4] M. Jahan, Q. Bao, K. P. Loh, *J. Am. Chem. Soc.* **2012**, *134*, 6707.
[5] Q. Lu, J. Rosen, Y. Zhou, G. S. Hutchings, Y. C. Kimmel, J. G. Chen, F. Jiao, *Nat. Commun.* **2014**, *5*, 3242.
[6] M. H. Lee, K. Takei, J. Zhang, R. Kapadia, M. Zheng, Y. Z. Chen, J. Nah, T. S. Matthews, Y. L. Chueh, J. W. Ager, A. Javey, *Angew. Chem. Int. Ed.* **2012**, *51*, 10760.
[7] M. R. Dubois, D. L. Dubois, *Acc. Chem. Res.* **2009**, *42*, 1974.
[8] Y. Kim, S. A. Shin, J. Lee, K. D. Yang, K. T. Nam, *Nanotechnology* **2014**, *25*, 342001.
[9] S. Park, C. W. Lee, M.-G. Kang, S. Kim, H. J. Kim, J. E. Kwon, S. Y. Park, C.-Y. Kang, K. S. Hong, K. T. Nam, *Phys. Chem. Chem. Phys.* **2014**, *16*, 10408.

[10] J. J. Concepcion, J. W. Jurss, J. L. Templeton, T. J. Meyer, *J. Am. Chem. Soc.* **2008**, *130*, 16462.
[11] J. Qiao, Y. Liu, F. Hong, J. Zhang, *Chem. Soc. Rev.* **2014**, *43*, 631.
[12] B. Kumar, M. Llorente, J. Froehlich, T. Dang, A. Sathrum, C. P. Kubiak, *Annu. Rev. Phys. Chem.* **2012**, *63*, 541.
[13] J. L. DiMeglio, J. Rosenthal, *J. Am. Chem. Soc.* **2013**, *135*, 8798.
[14] W. Zhu, R. Michalsky, Ö. Metin, H. Lv, S. Guo, C. J. Wright, X. Sun, A. A. Peterson, S. Sun, *J. Am. Chem. Soc.* **2013**, *135*, 16833.
[15] B. Kumar, J. M. Smieja, C. P. Kubiak, *J. Phys. Chem. C* **2010**, *114*, 14220.
[16] W. Yang, O. Auciello, J. E. Butler, W. Cai, J. A. Carlisle, J. E. Gerbi, D. M. Gruen, T. Knickerbocker, T. L. Lasseter, J. N. Russell, L. M. Smith, R. J. Hamers, *Nat. Mater.* **2002**, *1*, 253.
[17] C. R. Cabrera, H. D. Abruña, *J. Electroanal. Chem. Interfacial Electrochem.* **1986**, *209*, 101.
[18] B. Kumar, M. Asadi, D. Pisasale, S. Sinha-Ray, B. a Rosen, R. Haasch, J. Abiade, A. L. Yarin, A. Salehi-Khojin, *Nat. Commun.* **2013**, *4*, 2819.
[19] D. C. Grills, J. a Farrington, B. H. Layne, S. V Lymar, B. a Mello, J. M. Preses, J. F. Wishart, *J. Am. Chem. Soc.* **2014**, *136*, 5563.
[20] Y. Kou, Y. Nabetani, D. Masui, T. Shimada, S. Takagi, H. Tachibana, H. Inoue, *J. Am. Chem. Soc.* **2014**, *136*, 6021.
[21] S. K. Choi, U. Kang, S. Lee, D. J. Ham, S. M. Ji, H. Park, *Adv. Energy Mater.* **2014**, *4*, 1.
[22] J. H. Koh, H. S. Jeon, M. S. Jee, E. B. Nursanto, H. Lee, Y. J. Hwang, B. K. Min, *J. Phys. Chem. C* **2015**, *119*, 883.
[23] E. E. Benson, C. P. Kubiak, A. J. Sathrum, J. M. Smieja, *Chem. Soc. Rev.* **2009**, *38*, 89.
[24] K. Jin, J. Park, J. Lee, K. D. Yang, G. K. Pradhan, U. Sim, D. Jeong, H. L. Jang, S. Park, D. Kim, N.-E. Sung, S. H. Kim, S. Han, K. T. Nam, *J. Am. Chem. Soc.* **2014**, *136*, 7435.
[25] Y. Kim, D. Shin, W. J. Chang, H. L. Jang, C. W. Lee, H.-E. Lee, K. T. Nam, *Adv. Funct. Mater.* **2015**, *25*, 2345.
[26] G. Melaet, W. T. Ralston, C. S. Li, S. Alayoglu, K. An, N. Musselwhite, B. Kalkan, G. A. Somorjai, *J. Am. Chem. Soc.* **2014**, *136*, 2260.
[27] U. Sim, T.-Y. Yang, J. Moon, J. An, J. Hwang, J.-H. Seo, J. Lee, K. Y. Kim, J. Lee, S. Han, B. H. Hong, K. T. Nam, *Energy Environ. Sci.* **2013**, *6*, 3658.
[28] U. Sim, H.-Y. Jeong, T.-Y. Yang, K. T. Nam, *J. Mater. Chem. A* **2013**, *1*, 5414.
[29] Y. Zhao, N. C. Anderson, K. Zhu, J. A. Aguiar, J. A. Seabold, J. Oh, J. van de Lagemaat, H. M. Branz, N. R. Neale, *Nano Lett.* **2015**, *15*, 2517.
[30] K. Hirota, D. A. Tryk, T. Yamamoto, K. Hashimoto, M. Okawa, A. Fujishima, *J. Phys. Chem. B* **1998**, *102*, 9834.
[31] B. Aurian-Blajeni, I. Taniguchi, J. Bockris, *J. Electroanal. Chem. Interfacial Electrochem.* **1983**, *149*, 291.
[32] M. Bradley, T. Tysak, *J. Electroanal. Chem. Interfacial Electrochem.* **1982**, *135*, 153.
[33] R. Hinogami, Y. Nakamura, S. Yae, Y. Nakato, *J. Phys. Chem. B* **1998**, *102*, 974.
[34] T. J. LaTempa, S. Rani, N. Bao, C. A. Grimes, *Nanoscale* **2012**, *4*, 2245.
[35] J. Wu, R. M. Yadav, M. Liu, P. P. Sharma, C. S. Tiwary, L. Ma, X. Zou, X. Zhou, B. I. Yakobson, J. Lou, P. M. Ajayan, *ACS Nano* **2015**, *9*, 5364.
[36] S. Sen, D. Liu, G. T. R. Palmore, *ACS Catal.* **2014**, 3091.
[37] K. P. Kuhl, E. R. Cave, D. N. Abram, T. F. Jaramillo, *Energy Environ. Sci.* **2012**, *5*, 7050.
[38] Y. Hori, A. Murata, R. Takahashi, *J. Chem. Soc. Faraday Trans. 1* **1989**, *85*, 2309.
[39] Y. Hori, *Modern Aspects of Electrochemicstry*, Springer, New York, USA, **2008**, p. 89.
[40] B. Kumar, J. M. Smieja, A. F. Sasayama, C. P. Kubiak, *Chem. Commun.* **2012**, *48*, 272.
[41] Y. Chen, C. W. Li, M. W. Kanan, *J. Am. Chem. Soc.* **2012**, *134*, 19969.
[42] W. Zhu, Y.-J. Zhang, H. Zhang, H. Lv, Q. Li, R. Michalsky, A. A. Peterson, S. Sun, *J. Am. Chem. Soc.* **2014**, *136*, 16132.
[43] D. Kim, S. Lee, J. D. Ocon, B. Jeong, J. K. Lee, J. Lee, *Phys. Chem. Chem. Phys.* **2015**, *17*, 824.
[44] J. Bockris, J. C. Wass, *Mater. Chem. Phys.* **1989**, *22*, 249.
[45] S. Zhang, P. Kang, S. Ubnoske, M. K. Brennaman, N. Song, R. L. House, J. T. Glass, T. J. Meyer, *J. Am. Chem. Soc.* **2014**, *136*, 7845.
[46] D. Pan, C. Xi, Z. Li, L. Wang, Z. Chen, B. Lu, M. Wu, *J. Mater. Chem. A* **2013**, *1*, 3551.
[47] X. Huang, Z. Yin, S. Wu, X. Qi, Q. He, Q. Zhang, Q. Yan, F. Boey, H. Zhang, *Small* **2011**, *7*, 1876.
[48] Z. Wang, X. Cao, J. Ping, Y. Wang, T. Lin, X. Huang, Q. Ma, F. Wang, C. He, H. Zhang, *Nanoscale* **2015**, 9394.
[49] X. Huang, X. Qi, F. Boey, H. Zhang, *Chem. Soc. Rev.* **2012**, *41*, 666.
[50] U. Sim, H.-Y. Jeong, T.-Y. Yang, K. T. Nam, *J. Mater. Chem. A* **2013**, *1*, 5414.
[51] J. Oh, T. G. Deutsch, H.-C. Yuan, H. M. Branz, *Energy Environ. Sci.* **2011**, *4*, 1690.
[52] Y. C. Lin, Y. Chen, A. Shailos, Y. Huang, *Nano Lett.* **2010**, *10*, 2281.
[53] Y. Qu, L. Liao, Y. Li, H. Zhang, Y. Huang, X. Duan, *Nano Lett.* **2009**, *9*, 4539.
[54] C. W. Li, M. W. Kanan, *J. Am. Chem. Soc.* **2012**, *134*, 7231.
[55] L. G. Bulusheva, A. V. Okotrub, I. A. Kinloch, I. P. Asanov, A. G. Kurenya, A. G. Kudashov, X. Chen, H. Song, *Phys. Status Solidi (B)* **2008**; Vol. *245*, pp. 1971.
[56] C. Gómez-Navarro, R. T. Weitz, A. M. Bittner, M. Scolari, A. Mews, M. Burghard, K. Kern, *Nano Lett.* **2007**, *7*, 3499.
[57] L. G. Cançado, A. Jorio, E. H. M. Ferreira, F. Stavale, C. A. Achete, R. B. Capaz, M. V. O. Moutinho, A. Lombardo, T. S. Kulmala, A. C. Ferrari, *Nano Lett.* **2011**, *11*, 3190.
[58] M. Zheng, S. Liu, J. Li, D. Qu, H. Zhao, X. Guan, X. Hu, Z. Xie, X. Jing, Z. Sun, *Adv. Mater.* **2014**, *26*, 3554.
[59] J. Peng, W. Gao, B. K. Gupta, Z. Liu, R. Romero-Aburto, L. Ge, L. Song, L. B. Alemany, X. Zhan, G. Gao, S. A. Vithayathil, B. a Kaipparettu, A. A. Marti, T. Hayashi, J. J. Zhu, P. M. Ajayan, *Nano Lett.* **2012**, *12*, 844.
[60] X. Li, S. P. Lau, L. Tang, R. Ji, P. Yang, *Nanoscale* **2014**, *6*, 5323.
[61] C. P. Kelly, C. J. Cramer, D. G. Truhlar, *J. Phys. Chem. B* **2007**, *111*, 408.
[62] Y. Dai, H. Long, X. Wang, Y. Wang, Q. Gu, W. Jiang, Y. Wang, C. Li, T. H. Zeng, Y. Sun, J. Zeng, *Part. Part. Syst. Charact.* **2014**, *31*, 597.
[63] A. D. Bochevarov, E. Harder, T. F. Hughes, J. R. Greenwood, D. A. Braden, D. M. Philipp, D. Rinaldo, M. D. Halls, J. Zhang, R. A. Friesner, *Int. J. Quantum Chem.* **2013**, *113*, 2110.
[64] C. Lee, W. Yang, R. G. Parr, *Phys. Rev. B* **1988**, *37*, 785.
[65] P. C. Hariharan, J. A. Pople, *Theor. Chim. Acta* **1973**, *28*, 213.
[66] A. V. Marenich, J. Ho, M. L. Coote, C. J. Cramer, D. G. Truhlar, *Phys. Chem. Chem. Phys.* **2014**, *16*, 15068.